energies

MDPI

Article

Numerical 3D Model of a Novel Photoelectrolysis Tandem Cell with Solid Electrolyte for Green Hydrogen Production

Giosuè Giacoppo [1], Stefano Trocino [1], Carmelo Lo Vecchio [1], Vincenzo Baglio [1], María I. Díez-García [2], Antonino Salvatore Aricò [1] and Orazio Barbera [1,*]

[1] CNR-ITAE, Via Salita S. Lucia Sopra Contesse 5, 98126 Messina, Italy
[2] Departament de Química Física i Institut Universitari d'Electroquímica, Universitat d'Alacant, Apartat 99, E-03080 Alicante, Spain
* Correspondence: orazio.barbera@itae.cnr.it

Abstract: The only strategy for reducing fossil fuel-based energy sources is to increase the use of sustainable ones. Among renewable energy sources, solar energy can significantly contribute to a sustainable energy future, but its discontinuous nature requires a large storage capacity. Due to its ability to be produced from primary energy sources and transformed, without greenhouse gas emissions, into mechanical, thermal, and electrical energy, emitting only water as a by-product, hydrogen is an effective carrier and means of energy storage. Technologies for hydrogen production from methane, methanol, hydrocarbons, and water electrolysis using non-renewable electrical power generate CO_2. Conversely, employing photoelectrochemistry to harvest hydrogen is a sustainable technique for sunlight-direct energy storage. Research on photoelectrolysis is addressed to materials, prototypes, and simulation studies. From the latter point of view, models have mainly been implemented for aqueous-electrolyte cells, with only one semiconductor-based electrode and a metal-based counter electrode. In this study, a novel cell architecture was numerically modelled. A numerical model of a tandem cell with anode and cathode based on metal oxide semiconductors and a polymeric membrane as an electrolyte was implemented and investigated. Numerical results of 11% solar to hydrogen conversion demonstrate the feasibility of the proposed novel concept.

Keywords: photoelectrochemical tandem cell; hydrogen production; hematite photoanode; numerical model; solid electrolyte membrane; metal oxide semiconductor

Citation: Giacoppo, G.; Trocino, S.; Lo Vecchio, C.; Baglio, V.; Díez-García, M.I.; Aricò, A.S.; Barbera, O. Numerical 3D Model of a Novel Photoelectrolysis Tandem Cell with Solid Electrolyte for Green Hydrogen Production. *Energies* **2023**, *16*, 1953. https://doi.org/10.3390/en16041953

Academic Editor: Attilio Converti

Received: 8 December 2022
Revised: 31 January 2023
Accepted: 6 February 2023
Published: 16 February 2023

1. Introduction

Increases in world population and human activities have led to a considerable growth in global energy demand, most of which is fulfilled using non-renewable sources. With a view to a sustainable future and to address global energy challenges, current research is shifting toward environmentally neutral technologies. Indeed, consuming sustainable energy sources such as hydropower, wind, solar, ocean, and geothermal seems to be the only way to reduce usage of fossil fuel-based sources. However, using renewable energy sources (RES) for large-scale, cost-effective energy production is still a difficult challenge. Continuous energy provision is incompatible with the intermittent nature of RES, so an energy storage medium is essential for implementing a carbon-neutral economy [1,2]. Of the renewable energy sources mentioned above, the potential of solar energy, to date, has not been sufficiently exploited and is likely to contribute significantly to a green future. Various approaches exist to directly convert solar energy into chemical energy, as in the case of batteries or by producing a storable, high-energy density fuel, such as hydrogen [3]. Although batteries have long been manufactured and used with energy efficiency approaching 90%, this technology suffers from energy losses and capacity degradation over time. In contrast, hydrogen has the potential to be an excellent energy carrier because of its high energy density (about 140 MJ/kg) and the possibility of being a fuel for internal combustion engines, turbines, and fuel cells.

It does not release any greenhouse gases, only water as a by-product; if generated using RES, it is environmentally friendly [1,2]. In the gaseous state, hydrogen is not found in nature; it can be extracted from plants, methane, methanol, and higher hydrocarbons. In particular, it can be obtained from water. Currently, it is produced through several thermochemical, greenhouse gas-generating methods. Production by conventional water electrolysis requires massive external electrical energy sources. This process is environmentally friendly only if the electricity comes from RES. Other water electrolysis technologies include bio-aided, carbon- or hydrocarbon-aided, and photoelectrochemical [2,4]. Water electrolysis can be obtained in a photoelectrochemical cell (PEC), a device capable of implementing this splitting using electricity directly converted from sunlight. It is composed of two electrodes immersed in an aqueous electrolyte or separated by a hydrated solid electrolyte, at least one of which consists of a semiconductor that is exposed to sunlight and capable of absorbing it. The two electrodes of a PEC can be configured as an n-type semiconductor photoanode and a working in-the-dark cathode, two semiconductors (an n-type photoanode and a p-type photocathode), or a p-type semiconductor photocathode and a working in-the-dark anode [4,5]. Using only one semiconductor electrode is a challenging, and, to date, no materials based on earth-abundant and cheap elements offer a reasonable solution. One solution to this is to use two semiconductors in a tandem configuration, where the electrodes are excited by the same light beam, with the second electrode receiving the radiation filtered by the first. This configuration optimizes sunlight and combines the photovoltage generated by the two electrodes. Several n-type semiconductors, including TiO_2, ZnO, $BiVO_4$, Ta_3N_5, WO_3, and Si, have been studied as anodes for water photoelectrolysis. They show good potential but, conversely, are characterized by a large bandgap and/or instability in solution. Among the n-type semiconductors, hematite (α-Fe_2O_3) is characterized by low valence band position, abundance, stability in aqueous solution, nontoxicity, and bandgap of about 1.9–2.2 eV. It can utilize up to 40% of solar radiation and achieve a solar-to-hydrogen conversion efficiency of up to 15.5% [6]. From an experimental point of view, Du et al. [7] studied the water oxidation performance of a hematite photoanode in a PEC, enhanced via Co doping and surface modification. Yang et al. [8] altered the electrode surface with catalysts to improve semiconductor efficiency using atomic deposition-growth of MnO_x on hematite. Wang et al. [9] used quick high-temperature annealing to enhance the performance of thin hematite layers on a TiO_2 nano-sheet. Deshmukh et al. [10] investigated the electrochemical behavior of ZnO nanorods in 1 M Na_2SO_4 solution, employing various electrochemical methods. Wang et al. [11] considered hematite nanorod films deposited on titanium foils and modified with phosphorous, to improve the photoelectrochemical process. Syrek et al. [12] deposited electrochemically Cu_2O thin films on FTO-coated glass (Flourine Thin Oxide) at three different temperatures, finding that the FTO/Cu_2O cathode synthesized at the highest temperature showed superior performance. Meda et al. [13] studied different techniques to produce nanostructured WO_3 photoanodes on transparent conducting oxides, considering the Santato-Augustynski formula. Finally, Kwon [14] proposed a simple and fast method for producing hierarchical nanostructure hematite using an ultraviolet-assisted process. Similar studies on materials were carried out in [15,16]. PEC prototyping with hematite photoanodes was performed by Lopes et al. [17]; they designed a PEC for testing different photoelectrode configurations; they investigated two semiconductors: tungsten trioxide and undoped hematite. Brinkert et al. [18] demonstrated that, under microgravity conditions, it is possible to produce hydrogen efficiently in a photoelectrochemical manner; this represents a possible alternative to the current space mission life-support technologies. Hogerwaard et al. [19] developed an integrated concentrated photovoltaic and photoelectrochemical hydrogen reactor. Vilanova et al. [20] developed a 50 cm^2 tandem PEC-PV cell named "CoolPEC" (compact, optimized, open light PEC cell). Recently, important progress has been made in the modelling and simulation-supported development of PECs. Three-dimensional multiphysics models capable of simulating photoelectrochemical processes have been used for this purpose, providing design criteria for semiconductors, electrocatalysts, and electrolytes.

Moreover, modelling highlighted the most feasible device architectures regarding efficiency, stability, and safety. Nevertheless, the need remains to model the more complex physical aspects (e.g., thermal effects and bubble formation) that can induce malfunctions [21]. In this context, Berger et al. [22] developed a one-dimensional model of PEC that is valid for "wired" and "wireless" architectures. Stevens et al. [23] presented a computational method to evaluate the hourly temperature profiles and solar-hydrogen efficiency to achieve an optical concentration of PECs during a typical year. Hankin et al. [24] presented a model with a hematite photoanode and platinized titanium cathode, reproducing the experimental photoelectrolysis values obtained with a device equipped with 0.1×0.1 m^2 electrodes of various geometries and architectures. Njoka et al. [25] developed a two-dimensional numerical model of a hematite photoelectrode in a two-chamber reactor separated by a proton-permeable membrane. By considering the light absorption, charge transport, and redox reactions, the model investigated the effects of materials, height, and electrolyte velocity on hydrogen and oxygen production. Xiang et al. [26] investigated a detailed geometric parameter in two cell designs for a photoelectrolysis system sustained by a water vapor feed. Walczak et al. [27] simulated an integrated photoelectrolysis system equipped with a WO_3/FTO/p+n Si anode, a Pt/TiO_2/Ti/n+p Si cathode, and a Nafion membrane separator. Harmon et al. [28] considering charge transport in semiconductor-electrolyte-based PEC solar cells, modelled using the drift-diffusion-Poisson equations, proposed numerical methods for their resolution. Other models with liquid electrolytes can also be found in the literature [29–33]. As seen in the above literature review, models have generally considered liquid electrolytes with a polymeric separator. This work studied a novel concept of tandem cells with non-precious materials and hydrated solid electrolytes. A solid polymer electrolyte has many advantages; indeed, a PEC works with only pure water, and no corrosive liquid electrolytes with recirculation/purification systems are needed. Moreover, active materials can be easily sandwiched to form a solid-state and simplified device. This model aims to simulate water splitting into H_2 and O_2 through photoelectrolysis, in view of subsequent prototyping of the PEC. The system consists of a PEC composed of four main components: the photoelectrodes, the water channels, the solid electrolyte alkaline membrane, and a cathodic diffusion layer. The numerical model calculates the 3D distribution of the fluid dynamic and electrochemical quantities, the polarization curve (I-V), and their correlation with the cell design. The local current source was analytically simulated using the Gartner formulation at the photoanode [34] and the Butler–Volmer at the photocathode. This tandem configuration makes good use of the incident sunlight and combines the photovoltage generated from the two electrodes. Notably, the simulation covers fluid-dynamic and chemical aspects (conservation and transport) that a 1D model does not consider.

2. Model Definition

The novel concept of a PEC in a tandem configuration was based on a sandwich of FTO-coated glass supporting a layer of Fe-based semiconductor (anode), a solid polymer alkaline membrane, and a CuO-based photocathode supported on a hydrophobic carbonaceous layer.

Once the photoelectrochemical cell is assembled and fed with distilled water, the incident sunlight is transmitted across the transparent FTO-coated glass layer and promotes the water-splitting reaction. The gaseous products, H_2 and O_2, are collected by the channels formed over the membrane surface at the cell outlet. As dehydrated hydrogen production represents one of the main goals of this research activity, a highly hydrophobic porous layer was considered, in conjunction with the photocathode, to accomplish this task. Indeed, a hydrophobic porous layer allows the collection of hydrogen gas only, which passes through the pores, while keeping the water inside the cell. This is usually constituted by carbonaceous-based materials (Figure 1).

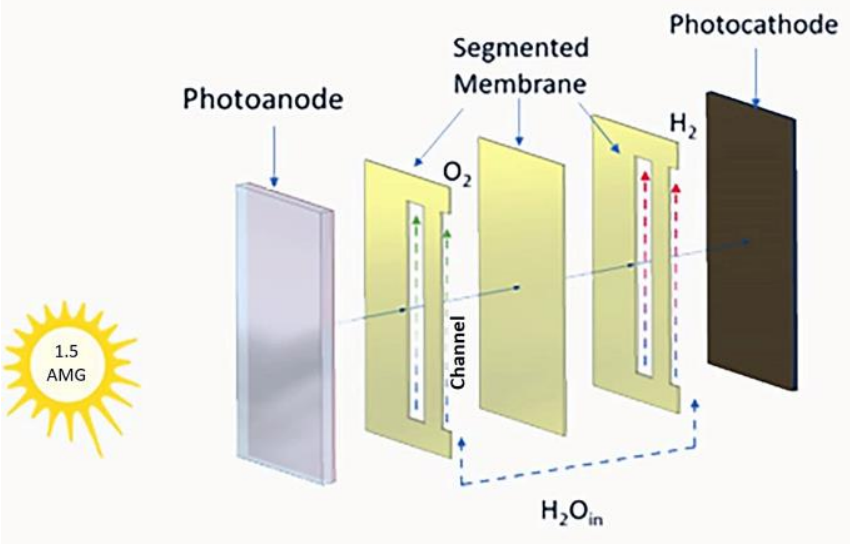

Figure 1. Sketch of the PEC novel concept.

Figure 2a shows the 3D single PEC model depicted in the simulation software. It consists of an anode collector (the transparent FTO-coated glass), a photoanode layer, a segmented membrane, a photocathode, a GDL (gas diffusion layer) for hydrogen collection, and a cathode collector. The segmented membrane performs three functions, it operates as a solid electrolyte, retains the water in the channels, and allows the escape of gaseous species. The PEC's elements are layered on each other, forming the geometric domain. They were parametrized in height and width in the x–z plane, according to Figure 2b; the length of the domain was defined along the y direction (Figure 2a).

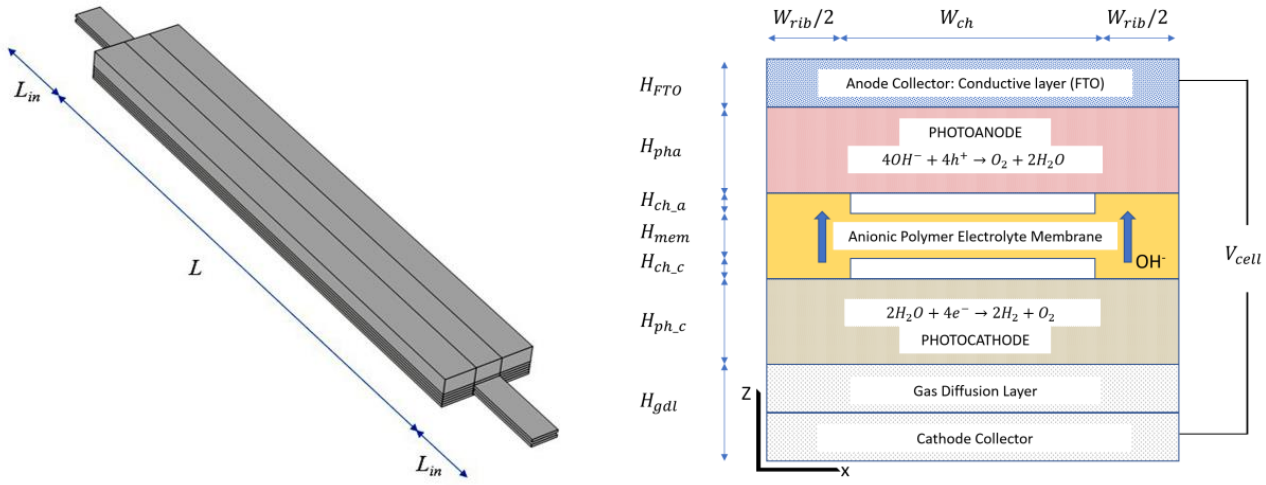

(**a**) (**b**)

Figure 2. (**a**) Drawing of the numerical 3D domain (**b**) PEC layers with their dimensional parameters (z–x plane).

Table 1 lists the geometric and reference physical characteristics of the numerical model.

Table 1. Geometrical parameters adopted for the model.

Name	Value	Description
L	10.0×10^{-3} m	Cell length
L_{in}	1.5×10^{-3} m	In/out length
H_{FTO}	4.0×10^{-3} m	Conductive layer height (FTO)
H_{pha}	4.0×10^{-8} m	Photoanode thickness
H_{ch_a}	5.0×10^{-5} m	Channel height
H_{mem}	1.0×10^{-4} m	Membrane thickness
H_{ch_c}	5.0×10^{-5} m	Channel height
H_{ph_c}	4.0×10^{-6} m	Photocathode thickness
H_{gdl}	3.0×10^{-4} m	GDL width
W_{ch}	5.0×10^{-4} m	Channel width
W_{rib}	1.2×10^{-3} m	Rib width
A_{inlet}	2.5×10^{-8} m^2	Inlet Area
A_{phele}	1.7×10^{-5} m^2	Photoelectrode Area
A_{cell}	1.7×10^{-5} m^2	Cell Area

A structured mesh (Figure 3) was implemented for the model discretization; the mesh was refined at the inlet, outlet, and central part of the active area, in correspondence with the channel considered for the escape of the reactants. The adopted mesh consisted of about 300,000 rectangular elements.

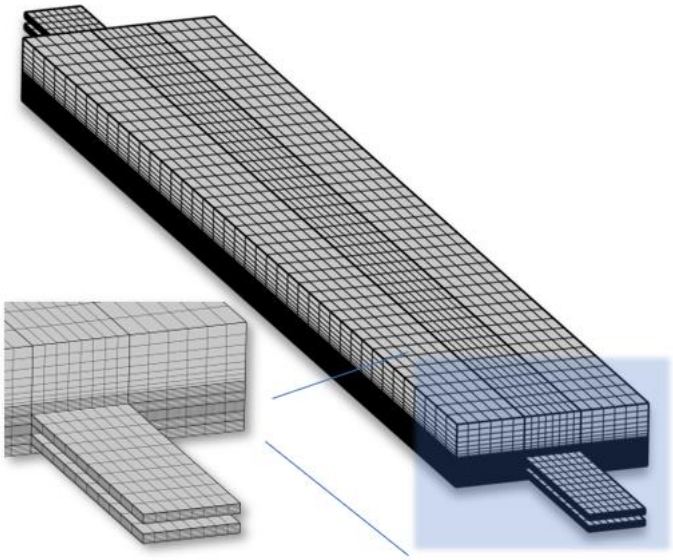

Figure 3. A picture of the mesh adopted for the model, the zoomed part (on the left) represents the inlet area with the refinement of the mesh.

Water is supplied through the anode and cathode sides of the simulated PEC and divided into H_2 and O_2 by the energy provided by the solar radiation (considered constant over the active surface) and the eventually applied bias E, with E < 1.23 V, under the semi-redox reactions below.

$$4OH^- + 4h^+ \rightarrow 2H_2O + O_2 \uparrow \text{(anodic)}$$

$$2H_2O + 2e^- \rightarrow 2OH^- + H_2 \uparrow \text{(cathodic)}$$

Produced and consumed species are transported through the anodic and cathodic channels and photoelectrodes. As the nanopillar structure characterizes the hematite photoanode, this layer should be porous (eventually with a low permeability), so the oxygen formed at the interface can pass through the photoanode and escape the PEC through the channels.

The main adopted model assumption was:

- Electrochemical reactions include the oxidation and reduction of water at the photoanode and cathode.
- Charge conservation within the electrolyte was assumed in the membrane, under the hypothesis that it is a homogeneous and continuous media, and no bubble generation effect was considered.
- Photocurrent densities were limited by the incident photon flux.
- Temperature effects were neglected. All the parameter values adopted here were evaluated at room temperature.

Comsol Multiphysics was used to implement the numerical simulations.

The model's inputs were the condition of the water flow entering the anode and the cathode, the operating pressure at the channel outlet (set as ambient pressure), and the voltage applied across the cell as the difference between the electrode potentials. The model calculates the ionic and electronic potential distribution, current density, velocity, pressure, and species distribution within the domain volume.

Table 2 reports the operating conditions for the base case, whilst Table 3 lists the model's physical parameters.

Table 2. Operating conditions of the model.

Name	Value	Description
p_{ref}	1.01×10^5 Pa	Reference pressure
T	308.15 K	Cell temperature
u_{in_anode}	5×10^{-4} m/s	Anode inlet flow velocity (Equations (1) and (2))
$u_{in\_cathode}$	5×10^{-4} m/s	Cathode inlet flow velocity (Equations (1) and (2))
μ_{anode}	1.19×10^{-5} Pa·s	Anode viscosity (Equations (2) and (3))
$\mu_{cathode}$	2.46×10^{-5} Pa·s	Cathode viscosity (Equations (2) and (3))
μ_{water}	7.972×10^{-4} Pa·s	Mixture viscosity (Equations (2) and (3))
ρ_{water}	1000 kg/m^3	Mixture density

Table 3. Model physical parameters.

Name	Value	Description
σ_{gdl}	222 S/m	GDL electric conductivity
σ_m	9.825 S/m	Membrane conductivity
w_{H2_in}	0.743	Inlet H_2 mass fraction (anode)
w_{H2O_in}	0.023	Inlet H_2O mass fraction (cathode)
w_{O2_in}	0.228	Inlet oxygen mass fraction (cathode)
M_{H2}	0.002 kg/mol	Hydrogen molar mass
M_{N2}	0.028 kg/mol	Nitrogen molar mass
M_{H2O}	0.018 kg/mol	Water molar mass
M_{O2}	0.032 kg/mol	Oxygen molar mass
c_{O2ref}	40.88 mol/m^3	Oxygen reference concentration (Equation (1))
c_{H2ref}	40.88 mol/m^3	Hydrogen reference concentration (Equations (1) and (11))

Table 3. *Cont.*

Name	Value	Description
D_{H2_H2O}	9.2048×10^{-5} m^2/s	H_2-H_2O binary diffusion coefficient (9.15×10^{-5}·(T/307.19)$^{1.75}$) (Equation (1))
D_{O2_H2O}	2.8208×10^{-5} m^2/s	O_2-H_2O binary diffusion coefficient (2.82×10^{-5}·(T/308.1)$^{1.75}$) (Equation (1))
V_{cell}	1.6 V	Cell voltage
ε_{gdl}	0.4	GDL porosity (Equation (3))
ε_l	0.3	Electrolyte phase volume fraction (Equation (3))
ε_{cl}	0.3	Open volume fraction for gas diffusion in porous electrodes ($1 - \varepsilon_l - \varepsilon_{GDL}$) (Equation (3))
k_{cl}	2.36×10^{-12} m^2	Permeability (porous electrode, $k_{\mathrm{GDL}}/5$, Equation (3))
k_{GDL}	1.18×10^{-11} m^2	GDL permeability (Equation (3))
i_{0_cat}	0.03 A/m^2	Cathode exchange current density (Equation (11))
V_{chan}	2.5×10^{-10} m^3	Channel volume
L_{in}	0.0015 m	Channel inlet length
α_{cat}	0.5	Cathode transfer coefficient (Equation (11))
q	1.61×10^{-19} C	Elemental charge (Equation (9))
E_{eq_a}	1.185 V	Anode equilibrium potential
$E_{fb,an}$	−0.7 V	Hematite flat band potential (Equation (9))
$E_{bp,cat}$	0	CuO flat band potential
Φ_0	3.8×10^{-18} m^{-2}·s^{-1} nm	Incident photon flux at 550 nm (Equation (9))
λ	5.5×10^{-7} m	Wavenumber length (Equation (10))
ε_0	8.854×10^{-12} F/m	Vacuum permittivity (Equation (9))
ε_{hema}	80	Hematite permittivity (Equation (9))
N_D	1×10^{25} 1/m^3	Donor concentration (Equation (9))
L_p	5×10^{-9} m	Diffusion length hematite
α_λ	5.879×10^6	Hematite extinction coefficient at 550 nm (Equation (10))
k	1	Kinetic constant (Equation (11))

2.1. Species Transport and Conservation

In the computational domains, conservation equations for mass, chemical species, momentum, and charge are solved. Diffusion and convection result in the transportation of species, which takes place in the channels, anodic, and cathodic photoelectrodes, and the GDL. In liquid water streams, the generated hydrogen and oxygen are considered diluted species. The species transportation was implemented using the molar balance equation:

$$\nabla \cdot (-D_i \nabla c_i) + \boldsymbol{u} \cdot \nabla c_i = 0 \quad (1)$$

In (1), D is the binary diffusion coefficient, c is the concentration, and $\boldsymbol{u}$ is the velocity vector. The first addend in (1) indicates the transport by diffusion according to Fick's law; the second is the convective transport caused by water flow. The anodic and cathodic fluxes are mixtures of two species (H_2O-O_2, H_2O-H_2); therefore, to consider the actual volume available for the diffusion of the species in the porous media, D is modified with Bruggeman's condition in the porous electrode domain. Porous materials can be considered a volume characterized by a solid matrix and voids, in which one or more fluid phases

can occur. In a porous medium, the theoretical and real diffusion coefficients are different. This occurs because the fluid has less transverse diffusion area available to it than the free volume. Since the fluid must move between the interstices of the solid matrix, it must travel a greater distance than to move geometrically between two points in the material itself, which makes the real concentration gradient lower than the theoretical one. By correlating the tortuosity of the path within the porous medium with the porosity, Bruggeman's theory allows the determination of the real diffusion coefficient to be used in Fick's law.

2.2. Flow Channels and Porous Electrodes

The Navier–Stokes Equation (2) describes the flow in the channels (anode and cathode):

$$\rho(\boldsymbol{u}\cdot\nabla\boldsymbol{u}) = \nabla\cdot\left[-p\boldsymbol{I} + \mu\left(\nabla\boldsymbol{u} + (\nabla\boldsymbol{u})^T\right)\right] \tag{2}$$

and Darcy Brinkman's Equation (3) gives the flow in the porous domains (photo-electrodes and GDL):

$$\frac{\rho}{\varepsilon}\left((\boldsymbol{u}\cdot\nabla)\frac{\boldsymbol{u}}{\varepsilon}\right) = \nabla\cdot\left[-p\boldsymbol{I} + \frac{\mu}{\varepsilon}\left(\nabla\boldsymbol{u} + (\nabla\boldsymbol{u})^T\right) - \frac{2}{3}\frac{\mu}{\varepsilon}(\nabla\cdot\boldsymbol{u})\boldsymbol{I}\right] - \left(\frac{\mu}{k} + \frac{Q}{\varepsilon^2}\right)\boldsymbol{u} \tag{3}$$

The momentum Equations (2) and (3) are solved together with the continuity Equation (4):

$$\rho\nabla\cdot\boldsymbol{u} = Q \tag{4}$$

In Equations (2)–(4), $\boldsymbol{u}$ represents the velocity, ρ is the fluid density, μ is the viscosity, p is the pressure, ε is the porosity, k is the permeability, Q is the mass flux, $\boldsymbol{I}$ is the identity tensor

2.3. Transportation and Conservation of Charge

Ohm's law, in conjunction with the charge balance for electrons and ions, is used to set the charge transport and conservation in photoelectrodes and electrolyte interfaces:

$$\nabla\cdot\boldsymbol{i_s} = 0 \tag{5}$$

$$\boldsymbol{i_s} = -\sigma_s\nabla\varphi_s \tag{6}$$

$$\nabla\cdot\boldsymbol{i_l} = 0 \tag{7}$$

$$\boldsymbol{i_l} = -\sigma_l\nabla\varphi_l \tag{8}$$

where $\boldsymbol{i_s}$ and $\boldsymbol{i_l}$ are the electronic and ionic current densities, respectively, and φ_s and φ_l are the electronic and ionic potentials, σ_s and σ_l the electronic and ionic conductivities. The flow of charged species is assumed to be dominated by the electric potential gradient instead of the concentration gradients. Considering the presence of liquid water in the channels, the membrane can be regarded as fully hydrated, and independent of external water flow, within certain conditions. Locally, at the photoelectrode–membrane interface, the electronic and ionic currents have the same order of magnitude, with the same number of electrons and ions exchanged in the redox half-reactions.

2.4. Photoelectrode Kinetics

Local current densities from sunlight were modelled using an analytical approach. The Gartner–Butler equation, a simplified equation arising from the Gartner model, was applied to the photoanode [35]:

$$\varphi_s - \varphi_l - E_{fb,an} = \left(\frac{N_D}{2\cdot q\cdot\varepsilon_{hema}\cdot\varepsilon_0}\right)\left(\frac{i_{loc,an}}{\alpha\Phi_0}\right)^2 \tag{9}$$

where φ_s and φ_l are the electronic and ionic potentials, $E_{fb,an}$ is the anode flat band potential, q is the elemental charge, N_D is the donor concentration, $i_{loc,an}$ is the local current density, Φ_0

is the incident photon flux, α is the absorption coefficient, which is related to the wavelength λ and extinction coefficient α_λ by:

$$\alpha = \frac{4\pi\alpha_\lambda}{\lambda} \tag{10}$$

For the photocathode case, a parametric equation with a form similar to that of the diffusion-limited Butler–Volmer equation was used as an approximation, so the local current $i_{loc,cat}$ is

$$i_{loc,cat} = i_{0,cat} \cdot \left(\frac{c_{H_2}}{c_{H_2,ref}} \right)^{k_{H_2}} \cdot \left[exp\left(\frac{\alpha_{cat} \cdot F \cdot \eta_{act,cat}}{RT} \right) - exp\left(\frac{-\alpha_{cat} \cdot F \cdot \eta_{act,cat}}{RT} \right) \right] \tag{11}$$

where $i_{0,cat}$ is the cathode exchange current density, c_{H_2} is the H_2 concentration, $c_{H_2,ref}$ is the H_2 reference concentration, F is the Faraday constant, R is the universal Gas constant, T is the temperature, $\eta_{act,cat}$ is the activation overpotential, α_{cat} is the charge transfer coefficient, and k_{H2} is the kinetic constant

3. Results and Discussion

Figure 4 shows the I–V curve obtained from the continuum model, varying the voltage applied at the cell leads. The figure reports the current density at two different values of the incident photon flux, because the model solves the equations specifically for monochromatic light. In this case, the incident photon flux corresponds to $\Phi_0 = 3.8 \times 10^{18}$ $\left[\mathrm{m}^{-2}\ \mathrm{s}^{-1}\ \mathrm{nm}\right]$ and corresponds to the energy content limited to just one wavelength number (λ = 550 nm). By increasing the incident photon flux up to $\Phi_0 = 5 \times 10^{21}$ $\left[\mathrm{m}^{-2}\ \mathrm{s}^{-1}\ \mathrm{nm}\right]$ (that corresponds to the total spectra), the current density magnitude increases accordingly. In the case of a monochromatic incident photon flux, the maximum value of current density was about 2.3 mA/cm^2; as expected, the full spectra generated a maximum current density of about 9.0 mA/cm^2

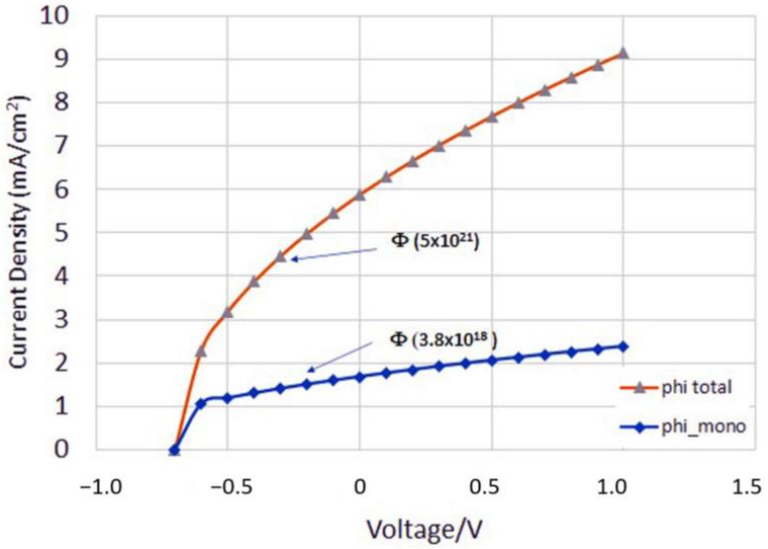

Figure 4. I–V curves derived from the continuum models and related to the total spectra and a monochromatic case.

The current density distribution in the electrodes (electronic current) and electrolyte (ionic current) is shown in Figure 5, which is illustrated as a cross-section of the PEC model.

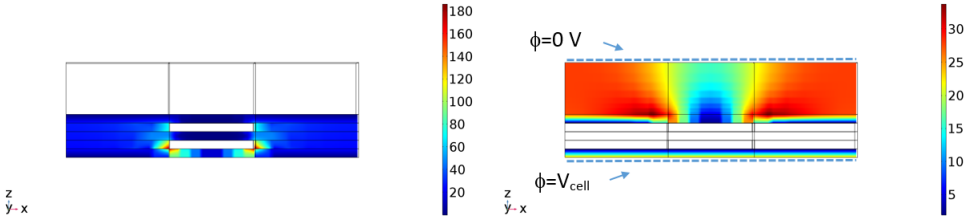

Figure 5. Current density ionic in the electrolyte (**left**) electronic in the photoelectrode (**right**) values in mA/cm^2.

The top and lower bound edges (on the anode side) show the highest achievable electrolyte current density. The three-phase boundary between the electrode, reactant, and the electrolyte is realized at this site. The reduced interface availability for the photo electrolysis process might be an issue for a scaled-up prototype. Therefore, the channel width and membrane rib width must be chosen appropriately, to maximize the surface for the reaction and minimize parasitic losses of the water and products entering/leaving the photoelectrochemical cell.

According to this trend, the photo-generated electronic current was characterized by the complementary tendency in the proximity of the current collection surfaces.

The current density field, as distributed, causes oxygen and hydrogen to form at the interface between the photoelectrodes and the water channels, as shown in Figure 6a.

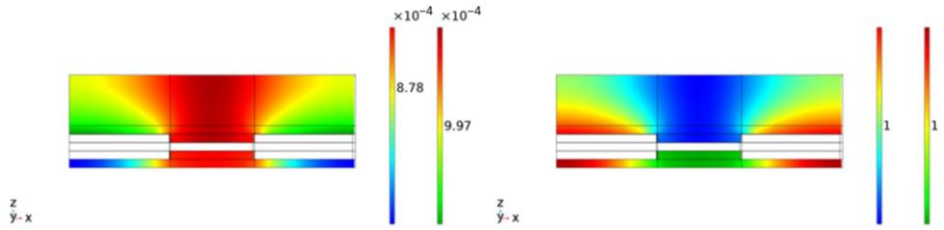

(**a**) (**b**)

Figure 6. (**a**) Mass fraction distributions of oxygen/hydrogen, (**b**) water consumed at both the anode and cathode side @ 1 V potential.

Specularly, water is consumed on both the anode and cathode sides (Figure 6b).

The results demonstrate how the presence of outlet channels for the gases produced and for the permanence of the water is essential for the proper functioning of the cell, and how modelling helps visualize this behavior. Using a continuous membrane, as often occurs in small laboratory cells as the cell area increases, implies the impossibility of escape for the oxygen and the difficulty, if not impossibility, of supplying of water for the solid electrolyte. This may negatively affect or even impede the device's proper functioning after a short time.

4. Conclusions

A new concept of PEC was numerically modelled using 3D multiphysics software, covering the physical (species and mass transport, heat transport, and charge transport) and electrochemical (electrode reactions) processes that occur as a result of sunlight. The numerical results showed that the cell could reach current densities in the 10 mA/cm^2 @ 1 V bias. Simulation results are helpful for cell design because they allow one to "visualize", albeit virtually, the nonuniform distribution of species, potentials, and currents that often cause significant performance reductions, especially in prototypes with a sizeable active surface area. In addition, they can be used as a tool to address the enhancement of the surface reactions and the cell configuration.

Further improvements of the continuum model are possible, for instance, with the explicit consideration of the losses caused by recombination.

Notwithstanding that Gartner's equation provides a good description of the photoelectrode–electrolyte interface in PEC cells, its limitations are well known, especially in not accounting for recombination effects, and thus are most evident in photoelectrolysis cells, where the slowness of redox processes, e.g., oxygen evolution, can become a determining factor in the rate of water molecule separation.

With the assumptions of Gartner's model, the polarization curve of the photoelectrolysis device can vary significantly. A simple way to eliminate these deviations might involve using explicit, potential-dependent formulations for the kinetic constants that appear in Equation (9).

Author Contributions: Conceptualization, G.G. and O.B.; methodology, G.G., O.B. and M.I.D.-G.; data curation, S.T., C.L.V., V.B. and A.S.A.; writing—original draft, G.G. and O.B.; writing—review and editing, G.G. and O.B. All authors have read and agreed to the published version of the manuscript.

Funding: This research was funded by the European Union's Horizon 2020 research and innovation program under grant agreement ID 760930 (FotoH2 project).

Data Availability Statement: Not applicable.

Conflicts of Interest: The authors declare no conflict of interest.

References

1. Burton, N.A.; Padilla, R.V.; Rose, A.; Habibullah, H. Increasing the efficiency of hydrogen production from solar powered water electrolysis. *Renew. Sustain. Energy Rev.* **2021**, *135*, 110255. [CrossRef]
2. Saravanan, P.; Khan, M.R.; Yee, C.S.; Vo, D.V.N. An overview of water electrolysis technologies for the production of hydrogen. In *New Dimensions in Production and Utilization of Hydrogen*; Elsevier: Amsterdam, The Netherlands, 2020; pp. 161–190, ISBN 9780128195536.
3. Modestino, M.A.; Haussener, S. An Integrated Device View on Photo-Electrochemical Solar-Hydrogen Generation. *Annu. Rev. Chem. Biomol. Eng.* **2015**, *6*, 13–34. [CrossRef]
4. Chatterjee, P.; Ambati, M.S.K.; Chakraborty, A.K.; Chakrabortty, S.; Biring, S.; Ramakrishna, S.; Wong, T.K.S.; Kumar, A.; Lawaniya, R.; Dalapati, G.K. Photovoltaic/photo-electrocatalysis integration for green hydrogen: A review. *Energy Convers. Manag.* **2022**, *261*, 115648. [CrossRef]
5. Bak, T.; Nowotny, J.; Rekas, M.; Sorrell, C.C. Photo-electrochemical hydrogen generation from water using solar energy. Materials-related aspects. *Int. J. Hydrogen Energy* **2002**, *27*, 991–1022. [CrossRef]
6. Li, C.; Luo, Z.; Wang, T.; Gong, J. Surface, Bulk, and Interface: Rational Design of Hematite Architecture toward Efficient Photo-Electrochemical Water Splitting. *Adv. Mater.* **2018**, *30*, 1707502. [CrossRef] [PubMed]
7. Du, C.; Yang, J.; Yang, J.; Zhao, Y.; Chen, R.; Shan, B. An iron oxide -copper bismuth oxide photoelectrochemical cell for spontaneous water splitting. *Int. J. Hydrogen Energy* **2018**, *43*, 22807–22814. [CrossRef]
8. Yang, X.; Du, C.; Liu, R.; Xie, J.; Wang, D. Balancing Photovoltage Generation and Charge-Transfer Enhancement for Catalyst-Decorated Photoelectrochemical Water Splitting: A Case Study of the Hematite/MnOx Combination. *J. Catal.* **2013**, *304*, 86–91. [CrossRef]
9. Wang, D.; Chen, Y.; Zhang, Y.; Zhang, X.; Suzuki, N.; Terashima, C. Boosting photoelectrochemical performance of hematite photoanode with TiO_2 underlayer by extremely rapid high temperature annealing. *Appl. Surf. Sci.* **2017**, *422*, 913–920. [CrossRef]
10. Deshmukh, P.R.; Sohn, Y.; Shin, W.G. Chemical synthesis of ZnO nanorods: Investigations of electrochemical performance and photo-electrochemical water splitting applications. *J. Alloys Compd.* **2017**, *711*, 573–580. [CrossRef]
11. Wang, X.; Gao, W.; Zhao, Z.; Zhao, L.; Claverie, J.P.; Zhang, X.; Wang, J.; Liu, H.; Sang, Y. Efficient photo-electrochemical water splitting based on hematite nanorods doped with phosphorus. *Appl. Catal. B Environ.* **2019**, *248*, 388–393. [CrossRef]
12. Syrek, K.; Jażdżewska, M.; Kozieł, M.; Zaraska, L. Photoelectrochemical activity of Cu_2O electrochemically deposited at different temperatures. *J. Ind. Eng. Chem.* **2022**, *115*, 561–569. [CrossRef]
13. Meda, L.; Tozzola, G.; Tacca, A.; Marra, G.; Caramori, S.; Cristino, V.; Bignozzi, C.A. Photo-electrochemical properties of nanostructured WO3 prepared with different organic dispersing agents. *Sol. Energy Mater. Sol. Cells* **2010**, *94*, 788–796. [CrossRef]
14. Kwon, J.; Yeo, J.; Hong, S.; Suh, Y.D.; Lee, H.; Choi, J.H.; Lee, S.S.; Ko, S.H. Photoreduction Synthesis of Hierarchical Hematite/Silver Nanostructures for Photoelectrochemical Water Splitting. *Energy Technol.* **2016**, *4*, 271–277. [CrossRef]
15. Gao, J.; Sahli, F.; Liu, C.; Ren, D.; Guo, X.; Werner, J.; Jeangros, Q.; Zakeeruddin, S.M.; Ballif, C.; Grätzel, M.; et al. Solar Water Splitting with Perovskite/Silicon Tandem Cell and TiC-Supported Pt Nanocluster Electrocatalyst. *Joule* **2019**, *3*, 2930–2941. [CrossRef]
16. Heremans, G.; Bosserez, T.; Martens, J.A.; Rongé, J. Stability of vapor phase water electrolysis cell with anion exchange membrane. *Catal. Today* **2019**, *334*, 243–248. [CrossRef]
17. Lopes, T.; Dias, P.; Andrade, L.; Mendes, A. An innovative photoelectrochemical lab device for solar water splitting. *Sol. Energy Mater. Sol. Cells* **2014**, *128*, 399–410. [CrossRef]

18. Brinkert, K.; Richter, M.H.; Akay, Ö.; Liedtke, J.; Giersig, M.; Fountaine, K.T.; Lewerenz, H.J. Efficient solar hydrogen generation in microgravity environment. *Nat. Commun.* **2018**, *9*, 2527. [CrossRef]
19. Hogerwaard, J.; Dincer, I.; Naterer, G.F. Experimental investigation and optimization of integrated photovoltaic and photoelectrochemical hydrogen generation. *Energy Convers. Manag.* **2020**, *207*, 112541. [CrossRef]
20. Vilanova, A.; Lopes, T.; Spenke, C.; Wullenkord, M.; Mendes, A. Optimized photoelectrochemical tandem cell for solar water splitting. *Energy Storage Mater.* **2018**, *13*, 175–188. [CrossRef]
21. Xiang, C.; Weber, A.Z.; Ardo, S.; Berger, A.; Chen, Y.; Coridan, R.; Fountaine, K.T.; Haussener, S.; Hu, S.; Liu, R.; et al. Modellierung, Simulation und Implementierung von Zellen für die solargetriebene Wasserspaltung. *Angew. Chem.* **2016**, *128*, 13168–13183. [CrossRef]
22. Berger, A.; Newman, J. An Integrated 1-Dimensional Model of a Photoelectrochemical Cell for Water Splitting. *J. Electrochem. Soc.* **2014**, *161*, E3328–E3340. [CrossRef]
23. Stevens, J.C.; Weber, A.Z. A Computational Study of Optically Concentrating, Solar-Fuels Generators from Annual Thermal- and Fuel-Production Efficiency Perspectives. *J. Electrochem. Soc.* **2016**, *163*, H475–H484. [CrossRef]
24. Hankin, A.; Bedoya-Lora, F.E.; Ong, C.K.; Alexander, J.C.; Petter, F.; Kelsall, G.H. From millimetres to metres: The critical role of current density distributions in photo-electrochemical reactor design. *Energy Environ. Sci.* **2017**, *10*, 346–360. [CrossRef]
25. Njoka, F.; Ookawara, S.; Ahmed, M. Influence of design and operating conditions on the performance of tandem photoelectrochemical reactors. *Int. J. Hydrogen Energy* **2018**, *43*, 1285–1302. [CrossRef]
26. Xiang, C.; Chen, Y.; Lewis, N.S. Modeling an integrated photoelectrolysis system sustained by water vapor. *Energy Environ. Sci.* **2013**, *6*, 3713–3721. [CrossRef]
27. Walczak, K.; Chen, Y.; Karp, C.; Beeman, J.W.; Shaner, M.; Spurgeon, J.; Sharp, I.D.; Amashukeli, X.; West, W.; Jin, J.; et al. Modeling, simulation, and fabrication of a fully integrated, acidstable, scalable solar-driven water-splitting system. *ChemSusChem* **2015**, *8*, 544–551. [CrossRef]
28. Harmon, M.; Gamba, I.M.; Ren, K. Numerical algorithms based on Galerkin methods for the modeling of reactive interfaces in photoelectrochemical (PEC) solar cells. *J. Comput. Phys.* **2016**, *327*, 140–167. [CrossRef]
29. Haussener, S.; Xiang, C.; Spurgeon, J.M.; Ardo, S.; Lewis, N.S.; Weber, A.Z. Modeling, simulation, and design criteria for photoelectrochemical water-splitting systems. *Energy Environ. Sci.* **2012**, *5*, 9922–9935. [CrossRef]
30. Carver, C.; Ulissi, Z.; Ong, C.K.; Dennison, S.; Kelsall, G.H.; Hellgardt, K. Modelling and development of photoelectrochemical reactor for H_2 production. *Int. J. Hydrogen Energy* **2012**, *37*, 2911–2923. [CrossRef]
31. Qureshy, A.M.; Ahmed, M.; Dincer, I. Simulation of transport phenomena in a photo-electrochemical reactor for solar hydrogen production. *Int. J. Hydrogen Energy* **2016**, *41*, 8020–8031. [CrossRef]
32. Haussener, S.; Hu, S.; Xiang, C.; Weber, A.Z.; Lewis, N.S. Simulations of the irradiation and temperature dependence of the efficiency of tandem photoelectrochemical water-splitting systems. *Energy Environ. Sci.* **2013**, *6*, 3605. [CrossRef]
33. Andrade, L.; Lopes, T.; Ribeiro, H.A.; Mendes, A. Transient phenomenological modeling of photoelectrochemical cells for water splitting-Application to undoped hematite electrodes. *Int. J. Hydrogen Energy* **2011**, *36*, 175–188. [CrossRef]
34. Pleskov, Y.; Gurevic, Y. *Semiconductor Photoelectrochemistry*, 1st ed.; Consultants Bureau: New York, NY, USA; Springer: New York, NY, USA, 1986; ISBN 978-1468490800.
35. Butler, M.A. Photoelectrolysis and physical properties of the semiconducting electrode WO_2. *J. Appl. Phys.* **1977**, *48*, 1914–1920. [CrossRef]